International Journal of Remote Sensing, 2013
Vol. 34, Nos. 9–10, 3177–3192, http://dx.doi.org/10.1080/01431161.2012.716548

Taylor & Francis
Taylor & Francis Group

Evaluation of the surface urban heat island effect in the city of Madrid by thermal remote sensing

José A. Sobrino[a]*, Rosa Oltra-Carrió[a], Guillem Sòria[a], Juan Carlos Jiménez-Muñoz[a], Belén Franch[a], Victoria Hidalgo[a], Cristian Mattar[a], Yves Julien[a], Juan Cuenca[a], Mireia Romaguera[a], J. Antonio Gómez[b], Eduardo De Miguel[b], Remo Bianchi[c], and Marc Paganini[c]

[a]*Global Change Unit (GCU), Image Processing Laboratory (IPL), Parc Científic Universitat de València, E-46980 Paterna, Spain;* [b]*Instituto Nacional de Técnica Aerospacial, 28850 Torrejón de Ardoz, Spain;* [c]*European Space Agency (ESA), Earth Observation Programmes, Science, Applications and Future Technologies Department, I-00044 Frascati (RM), Italy*

(*Received 20 January 2011; accepted 11 May 2011*)

The surface urban heat island (SUHI) effect is defined as the increased surface temperatures in urban areas in contrast to cooler surrounding rural areas. In this article, the evaluation of the SUHI effect in the city of Madrid (Spain) from thermal infrared (TIR) remote-sensing data is presented. The data were obtained from the framework of the Dual-use European Security IR Experiment (DESIREX) campaign that was carried out during June and July 2008 in Madrid. The campaign combined the collection of airborne hyperspectral and *in situ* measurements. Thirty spectral and spatial high-resolution images were acquired with the Airborne Hyperspectral Scanner (AHS) sensor in a 11, 21, and 4 h UTC scheme. The imagery was used to retrieve the SUHI effect by applying the temperature and emissivity separation (TES) algorithm. The results show a nocturnal SUHI effect with a highest value of 5 K. This maximum value agrees within 1 K with the highest value of the urban heat island (UHI) observed using air temperature data (AT). During the daytime, this situation is reversed and the city becomes a negative heat island.

1. Introduction

The urban heat island (UHI) phenomenon is an example of modification of the atmosphere by urbanization (Oke 1981). The effect is characterized by the heating of urban zones in comparison with their non-urbanized surroundings. So, UHI is defined as the difference between the air temperature (AT) within the city and the AT of its surroundings. When the phenomenon is monitored with remote-sensing data, we have to talk about surface urban heat island (SUHI), as the parameter studied is no longer AT but the land surface temperature (LST). In this article, we present results for both phenomena in the city of Madrid (Spain).

There are several examples of experimental campaigns, the aim of which was to study the urban climate and in most of the cases to quantify the UHI of different urban zones. One strategy to achieve this purpose is to record AT, humidity, and wind speed measurements

*Corresponding author. Email: sobrino@uv.es

using fixed stations or mobile transects (Oke 1973; Voogt and Oke 1998; Fernández et al. 2004; Najjar et al. 2004; Jasche and Rezende 2007; Masson et al. 2008). Many other studies applied remote-sensing technology, using satellite images (Voogt and Oke 2003; Hartz et al. 2006; Li et al. 2009; Stathopoulou et al. 2009) or airborne sensor imagery (Voogt and Oke 1997; Lagourade et al. 2004; Masson et al. 2008), to describe the behaviour of urban surfaces.

Regarding the city of Madrid, UHI has been studied using AT data under the urban canopy from mobile transects (Yagüe, Zurita, and Martinez 1991; Fernández et al. 2004) and also using satellite images (Pérez-González, García-Rodríguez, and Guerra-Zaballos 2003). However, the intensive Dual-use European Security IR Experiment (DESIREX) carried out in Madrid in 2008 went far, providing for the first time a large number of ground measurements (fixed and mobile) and high-resolution airborne thermal data (Sobrino et al. 2009); hence, both effects, SUHI and UHI, can be evaluated and correlations between them can be established. The DESIREX campaign was developed in the framework of the Earth Observation Programmes of the European Space Agency (ESA) that carry out a set of ground-based and airborne campaigns to support geophysical algorithm development, calibration/validation, and the simulation of future spaceborne Earth observation missions for application development related to land, oceans, and atmosphere.

2. Study area

The chosen test area for data collection is located in the city of Madrid. Madrid is the capital and largest city of Spain. It is located in a relatively flat area about 50 km south of the Spanish Central Ridge. The main topographic feature is River Manzanares, which crosses the city roughly from west to east. The Manzanares valley causes a small, narrow depression with shoulders rising approximately 75 m to the north and less than 50 m to the south. A secondary feature is a small valley from a tributary stream (Arroyo del Abroñigal, now buried below the M-30 road), that crosses the city from north to south, joining the Manzanares in the Nudo Sur area of the city. This valley has a depth of 25–30 m. It is important to note that both valleys work frequently as channels for air masses from the cooler northern rural areas. The city districts not affected by the valley slopes are fairly flat, with a gentle slope to the north and to the east, so that the maximum city height is located in the northern limit of the city, topping roughly 700 m above sea level, while the lower occurs in the River Manzanares around 550 m. The population of the city is 3.2 million (January 2008), while the estimated urban area population is 5.1 million. The city spans a total of 607 km^2. Madrid has a temperate Mediterranean climate with cool winters with temperatures that sometimes drop below 0°C. Summer tends to be hot with temperatures that consistently surpass 30°C in July and that can often reach 40°C. Summer and winter are the driest seasons, with most rainfall occurring in the autumn and spring. The coordinates of the centre of the test area are 40° 23′ N, 3° 43′ W.

3. Data

3.1. Atmospheric data

Two balloons per day were launched at noon and at midnight to characterize water vapour vertical profiles. For each flight day, four captive balloon soundings were taken at the city centre. Lidar measurements and meteorological data were acquired to characterize aerosol vertical profiles. The meteorological network stations of Madrid City Council provided data of wind direction, wind speed, solar radiation, relative humidity, atmospheric pressure, AT, and precipitation.

3.2. Land surface data

Calibration and validation activities were carried out simultaneously with the Airborne Hyperspectral Scanner (AHS) and Advanced Spaceborne Thermal Emission and Reflection Radiometer (ASTER) overpasses. CIMEL CE312 (CIMEL, Paris, France), RAYTEK MID (RAYTEK, Santa Cruz, CA, USA), and Heitronics radiometers (Heitronics, Wiesbaden, Germany) and the NEC TH9100 thermal camera (NEC, Tokyo, Japan) were used in the thermal domain for measuring downward atmospheric radiance, surface radiometric temperature, and emissivity, and the ASD FieldSpec3 (ASD, Boulder, CO, USA) and GER 1500 (GER, Poughkeepsie, NY, USA) spectroradiometers in the solar range for reflectivity measurements. Different natural and artificial surfaces were selected to obtain their spectral reflectance signature using the ASD FieldSpec3 and GER 1500 spectroradiometers, with the aim to make a spectral library of representative urban materials. The emissivities of the different surfaces were also obtained using the CIMEL-CE312-2 radiometer by means of the temperature and emissivity separation (TES) algorithm (Gillespie et al. 1998). Surfaces analysed were green grass, bare soil, brick, pavement, concrete, asphalt composition, tile, asphalt, metallic mesh, steel, asbestos, and steel.

3.3. Fixed masts

Fixed masts were set up for continuous measurements in rural (over green grass surface), urban-medium, and urban-dense spots in Madrid during the DESIREX campaign (Figure 1). AT, relative humidity, and ground radiometric temperature were acquired in six masts. Wind speed and direction were also available in some of the stations. Radiation balance measurements were carried out for two fixed masts, one in a rural zone and other in an urban-dense zone, using two pyranometers (for the solar range) and two pyrgeometers (for the longwave term), one pointing up and the other pointing down.

3.4. Airborne instrumentation

The AHS sensor is an airborne imaging 80-band radiometer, developed and built by SensyTech Inc. (currently Argon ST (Fairfax, VA, USA), and formerly Daedalus Ent. Inc.).

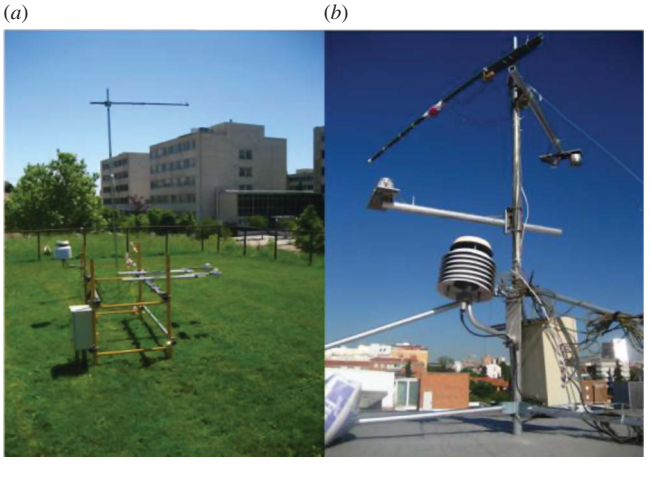

Figure 1. Fixed masts. (*a*) Rural area. (*b*) Urban area.

It is the property of *Instituto Nacional de Técnica Aeroespacial* (INTA) and is operated by technical staff of its Remote Sensing Lab. The AHS is a line scanner with a concept shared with classical airborne line scanners, such as the Airborne Thematic Mapper (ATM), Multispectral Infrared and Visible Imaging Spectrometer (MIVIS), and Moderate Resolution Imaging Spectroradiometer (MODIS) Airborne Simulator (MAS). The sensor is installed in the INTA's C-212 200 EC-DUQ airplane and is integrated with a GPS-INS POS/AV 410 V5 provided by Applanix (Richmond Hill, ON, Canada).

The AHS spectrometer is configured with very distinct spectral performances depending on the spectral region considered. It contains four types of detectors organized in five optical ports (Table 1). Port 1 covers the visible/near-infrared (VIS/NIR) range. Its bands are relatively broad (28–30 nm wide). The spectral coverage is continuous from 443 nm up to 1025 nm. In the short-wave infrared (SWIR) range, port 2A has an isolated band centred at 1.6 μm and 90 nm wide, which is used to simulate the corresponding spectral channel that can be found in a number of satellite missions. Next, port 2 has a set of continuous, fairly narrow bands (17–18 nm wide) laying between 1907 and 2558 nm, which are well suited for soil/geologic studies. In the medium-wave infrared (MWIR) region, port 3 with seven bands operating from 3.1 to 5.5 μm gathers the energy through an indium antimonide (InSb) 7-element detector array cooled with liquid nitrogen. The mean bandwidth is 350 nm. The long-wave infrared (LWIR) photons, from 8.1 to 13.4 μm, are collected by optical port 4, with a 10-element mercury cadmium telluride (MCT) detector array that needs as well to be kept at cryogenic temperature to optimize its performance. The average bandwidth is now 480 nm. The spectral arrangement of the AHS thermal bands is given in Table 2.

Electronic signals coming from the detectors, preamplifiers, and amplifiers are digitized at 12 bits and sampled every 2.1 mrad along the field of view (FOV) (90° or 1.57 rad), which

Table 1. AHS spectral configuration for DESIREX 2008.

	Port 1	Port 2A	Port 2	Port 3	Port 4
Spectral coverage (μm)	0.443–1.025	1.55–1.65	1.90–2.55	3.3–5.4	8.2–13.4
FWHM (nm) (average)	29	90	17	300	450
Number of bands	20	1	42	7	10

Note: FWHM, full width at half maximum.

Table 2. AHS thermal bands (Port 4) during the DESIREX 2008 experimental campaign.

Band	Effective wavelength (μm)
71	8.18
72	8.66
73	9.15
74	9.60
75	10.07
76	10.59
77	11.18
78	11.78
79	12.35
80	12.93

results in 750 pixel samples per scan line. The AHS instantaneous field of view (IFOV) determined by a square field stop placed in the middle of its optical path is 2.5 mrad.

Radiometric calibration is achieved by at-lab measurements looking at an integrating sphere for the reflective channels (port 1, port 2A, and port 2). Nevertheless the radiometric response of the emissive detectors, port 3 and port 4, is calibrated comparing the signal gathered by the detectors when looking to the known reference thermal sources integrated in the scan head frame: two black bodies the sensor looks at every scan line, before and after each scan line is collected.

Two more features are implemented to enlarge the dynamic range of the emissive infrared detectors: a bilinear amplification curve that provides lower gain at high radiance levels and a set of thermal attenuating filters that can be placed at the entrance of the TIR ports to prevent detector saturation when looking at high-temperature targets.

3.4.1. Imagery data set

During the DESIREX experimental campaign, the AHS flights took place on 25, 26, and 28 June and on 1, 2, and 4 July, with a total of 30 AHS images divided into two different patterns, one from northwest (Geographic Latitude/Longitude (Datum WGS84): N 40°28′48.8″/W 3°48′15.2″) to southeast (Geographic Latitude/Longitude (Datum WGS84): N 40°20'56.0″/W 3°33′53.5″) (named hereinafter flight P01) and the other from south (Geographic Latitude/Longitude (Datum WGS84): N 40°16′57.4″/W 3°41′50.9″) to north (Geographic Latitude/Longitude (Datum WGS84): N 40°33′42.3″/W 3°41′7.3″) (named hereinafter flight P02). These give a total length of roughly 1000 km along track recorded data at different flight altitudes (1641, 2497, and 3409 m above sea level) and at different times (at noon, at midnight, and before Sun rising). The description of the different flights is given in Table 3.

4. LST retrieval

4.1. Atmospheric correction

Atmospheric correction of the AHS visible and near-infrared (VNIR) data (bands from 1 to 20) was evaluated from the following radiative transference equation:

$$L_{\text{sensor}} = \left[\rho_{\text{so}} + \frac{(\tau_{\text{ss}} + \tau_{\text{sd}})\,\rho_{\text{surf}}\tau_{\text{do}}}{1 - \rho_{\text{surf}}\rho_{\text{dd}}}\right]\frac{E_{\text{s}}}{\pi} + \frac{(\tau_{\text{ss}} + \tau_{\text{sd}})}{1 - \rho_{\text{surf}}\rho_{\text{dd}}}\frac{E_{\text{s}}}{\pi}\rho_{\text{surf}}\tau_{\text{oo}}, \tag{1}$$

where L_{sensor} is the radiance at sensor level, E_{s} is the direct solar irradiance, ρ_{so} is the bidirectional reflectivity of the atmospheric layer, τ_{ss} is the downwelling direct transmittance, τ_{sd} is the diffuse transmittance in the solar direction, τ_{do} is the diffuse transmittance in the viewing direction, ρ_{dd} is the atmospheric spherical albedo, τ_{oo} is the upwelling direct transmittance, and ρ_{surf} is the surface reflectivity.

Thus, the surface reflectivity can be obtained according to

$$\rho_{\text{surf}} = \frac{\rho_{\text{TOA}} - \rho_{\text{so}}}{(\tau_{\text{do}} + \tau_{\text{oo}})\,(\tau_{\text{ss}} + \tau_{\text{sd}}) + \rho_{\text{dd}}\,(\rho_{\text{TOA}} - \rho_{\text{so}})}. \tag{2}$$

ρ_{TOA}, the top of atmoshpere reflectivity, and the atmospheric parameters are obtained using the radiative transference code Moderate Resolution Atmospheric Transmission

Table 3. Description of the AHS flights carried out during DESIREX 2008.

Date (ddmmyy)	Time (UTC)	Flight ID	Altitude (m above sea level)	Pixel size (m)
25 June 2008	11:11	P01I1	2497	4
25 June 2008	11:27	P02I1	2497	4
25 June 2008	22:15	P01I2	2497	4
25 June 2008	22:31	P02I2	2497	4
26 June 2008	04:12	P01ID	2497	4
26 June 2008	04:26	P02ID	2497	4
28 June 2008	11:32	P01I1	2497	4
28 June 2008	11:53	P02I1	2497	4
28 June 2008	12:13	P01AD	3409	6
28 June 2008	12:31	P02AD	3409	6
28 June 2008	20:57	P01BD	1641	2
28 June 2008	21:12	P02BD	1641	2
28 June 2008	21:29	P01I2	2497	4
28 June 2008	21:44	P02I2	2497	4
1 July 2008	11:21	P01I1	2497	4
1 July 2008	11:44	P02I1	2497	4
1 July 2008	21:01	P01BD	1641	2
1 July 2008	21:15	P02BD	1641	2
1 July 2008	21:29	P01SD	1641	2
1 July 2008	21:43	P02SD	1641	2
1 July 2008	21:59	P01I2	2497	4
1 July 2008	22:12	P02I2	2497	4
2 July 2008	04:09	P01ID	2497	4
2 July 2008	04:26	P02ID	2497	4
4 July 2008	11:16	P01I1	2497	4
4 July 2008	11:32	P02I1	2497	4
4 July 2008	21.59	P01I2	2497	4
4 July 2008	22:14	P02I2	2497	4
4 July 2008	22:40	P01AD	3409	6
4 July 2008	22:55	P02AD	3409	6

(MODTRAN) 4.3 (Berk et al. 2003) following Verhoef and Bach's (2003) methodology. The water vapour was obtained from *in situ* radiosoundings launched almost simultaneously with the AHS overpass, and the aerosol optical thickness following the method of Guanter, Gomez-Chova, and Moreno (2008).

Atmospheric correction of the AHS TIR bands (71–80) was performed considering (Sobrino et al. 2008):

$$L_i(T_i) = L_i^{\mathrm{LLR}}\tau_i + L_i^{\uparrow}, \tag{3}$$

where $L_i(T_i)$ is the radiance measured by channel i of the sensor (T_i is the at-sensor brightness temperature in channel i), τ_{i} is the atmospheric transmissivity of the surface-sensor path, and $L_i^{\uparrow}$ is the upwelling path radiance. The term L_i^{LLR} is the land-leaving radiance (LLR) or radiance measured at ground level, which is given by:

$$L_i^{\mathrm{LLR}} = \varepsilon_i B_i(T_{\mathrm{s}}) + (1-\varepsilon_i)\frac{F_i^{\downarrow}}{\pi}, \tag{4}$$

where ε_i is the surface emissivity in channel i, $B_i(T_s)$ is the Planck radiance at surface temperature T_s, and $F_i^{\downarrow}$ is the downwelling sky irradiance. In (4), the assumption of the Lambertian behaviour for the surface was considered in order to express the reflection term as $(1-\varepsilon_i)(F_i^{\downarrow}/\pi)$. The magnitudes involved in Equations (3) and (4) are band-averaged values using the spectral response functions and also depend on the observation angle. Then, the atmospheric correction in the TIR region is reduced to:

$$L_i^{\mathrm{LLR}} = \frac{L_i(T_i) - L_i^{\uparrow}}{\tau_i}. \tag{5}$$

The atmospheric parameters τ_i, $F_i^{\downarrow}$, and $L_i^{\uparrow}$ involved in the above equation were estimated using MODTRAN-4 and *in situ* radiosoundings launched almost simultaneously with the AHS overpass. Channel values were finally obtained using AHS TIR band filter functions. Sobrino et al. (2008) showed that AHS bands 71 and 80, located around 8 and 13 μm, respectively, present the highest atmospheric absorption, whereas band 74 is located in the region of ozone absorption (even though at the altitude of the AHS flights, this absorption is not observed). Therefore, the *a priori* optimal bands for TIR remote sensing from AHS thermal channels are 72, 73, 75, 76, 77, 78, and 79.

4.2. *Vicarious calibration of the AHS thermal bands*

Before the application of algorithms, it is convenient to compare the data provided by the sensor with the data acquired *in situ*. According to Tonooka et al. (2005), the conditions required for calibration sites are (1) targets should be homogeneous in both surface temperature and emissivity and (2) atmospheric conditions should be stable and cloud free, with a small total amount of water vapour. This has been made for 11 test points on water and green grass.

At-sensor radiances for each AHS TIR band were reproduced from ground-based measurements using Equations (3) and (4). Surface temperatures were obtained from measurements *in situ*. Emissivity spectra for water and green grass were extracted from the ASTER Spectral Library (http://speclib.jpl.nasa.gov). Figure 2 shows the AHS band emissivities for both surfaces considered.

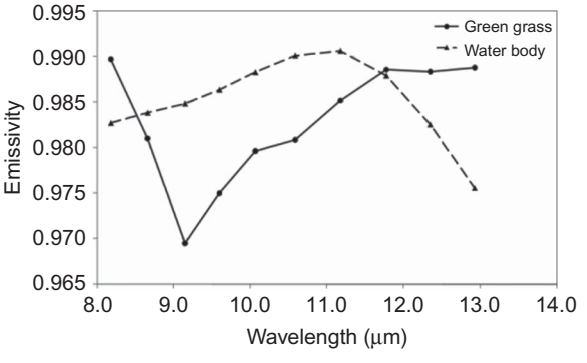

Figure 2. Emissivity values for the 10 AHS TIR bands used in the vicarious calibration obtained from emissivity spectra included in the ASTER Spectral Library.

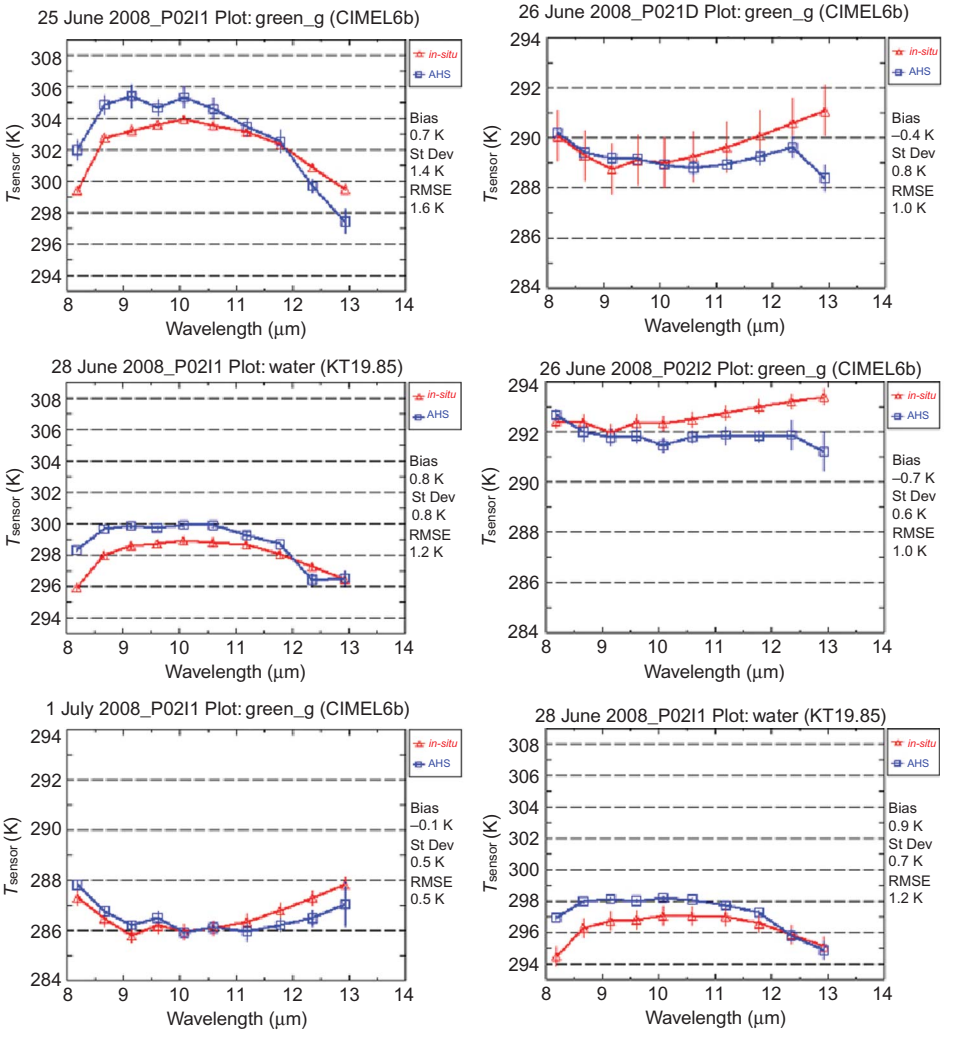

Figure 3. Comparison between the at-sensor brightness temperatures, T_{sensor}, measured with the 10 AHS TIR bands and the temperatures reproduced from ground-based measurements (*in situ*). Error bars for '*in situ*' values refer to the standard deviation of the different field measurements collected near the AHS overpass, and error bars for 'AHS' values refer to the standard deviation of a sample of 3 pixels × 3 pixels. The tops of the graphs show date (ddmmyy), flight ID (see Table 3), plot (water for water surface and green_g for green grass surface), and name of the field radiometer used to measure the surface temperature (in parentheses). Bias, standard deviation (St Dev), and root mean square errors (RMSEs) are given.

Examples of the comparison between at-sensor values measured with the AHS bands and those reproduced from ground-based measurements are shown in Figure 3 for different AHS images. The comparison is presented in terms of at-sensor brightness temperatures. The shape of the spectra obtained from ground-based measurements agrees with those extracted from the AHS images, which indicates the good performance of the AHS TIR bands.

Table 4. Statistical values from the vicarious calibration of AHS TIR bands.

Date (ddmmyy)	Time (UTC)	Instrument	Plot	Bias (K)	σ (K)	RMSE (K)
25 June 2008	11:27	CIMEL	Green grass	0.8	1.5	1.7
25 June 2008	22:31	CIMEL	Green grass	0.02	0.6	0.6
26 June 2008	04:26	CIMEL	Green grass	−0.5	0.9	1.0
28 June 2008	11:53	CIMEL	Green grass	−0.1	1.4	1.4
28 June 2008	11:53	Heitronics	Water	0.9	0.9	1.3
28 June 2008	11:53	Raytek	Water	0.1	0.9	0.9
28 June 2008	21:44	CIMEL	Green grass	−0.8	0.7	1.0
1 July 2008	11:44	Heitronics	Water	0.2	0.9	0.9
1 July 2008	22:12	CIMEL	Green grass	−0.1	0.5	0.5
2 July 2008	04:26	CIMEL	Green grass	−0.2	0.7	0.8
4 July 2008	11:32	Heitronics	Water	1.0	0.8	1.3
All days	All measures	All instruments	All surfaces	0.1	1.0	1.0

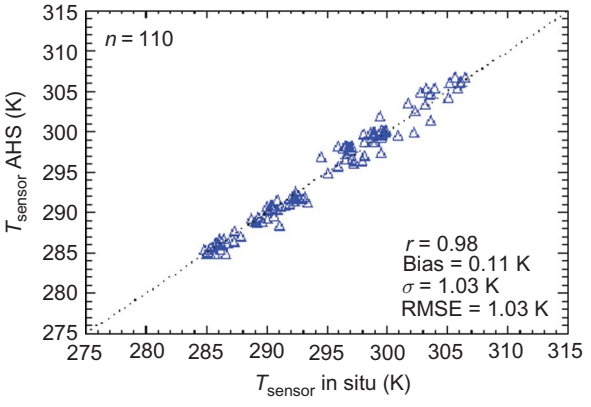

Figure 4. Comparison between the at-sensor brightness temperatures reproduced from ground-based measurements (T_{sensor} (*in situ*)) and the those extracted from the AHS images (T_{sensor} (AHS)).

The results for all test points are summarized in Table 4. We can observe that the root mean square error (RMSE) values are bigger during daytime than at night; this is due to the thermal homogeneity at night. A RMSE of 1.0 K and a Bias of 0.1 K are obtained for the 11 test points and for the 10 AHS TIR bands considered. Finally, Figure 4 displays the results obtained for the 11 points for each of the 10 AHS TIR channels considered.

4.3. The TES algorithm

LST and land surface emissivity (LSE) were retrieved from TIR AHS bands by applying the TES algorithm described in Gillespie et al. (1998). TES solves the problem of coupling between LST and LSE that appears when the radiative transfer equation (Equation (3)) is applied to each thermal band of a multispectral sensor. TES is divided into three modules (Normalized Emissivity Method (NEM), Ratio, and maximum – minimum difference (MMD)). The algorithm uses atmospherically corrected radiances and downwelling atmospheric radiance as input. After the NEM and Ratio modules, a β spectrum of relative

emissivities is obtained. Finally in the MMD module, a semi-empirical relationship, determined from laboratory spectra, is used between the minimum emissivity ($\varepsilon_{\min}$) and the spectral contrast (MMD). This relationship is different for each sensor and for each spectral band configuration. In this way, the emissivity for each thermal band is retrieved using Equation (6) and the LST is obtained by inversion of Planck's law at the thermal band *i*, for which the emissivity is maximum:

$$\varepsilon_i = \beta_i \left[\frac{\varepsilon_{\min}}{\min(\beta_i)} \right], \tag{6}$$

where β_i is the relative emissivity obtained from the Ratio module. In this article, TES has been applied to seven of the 10 thermal bands of the AHS sensor, specifically bands 72, 73, 75, 76, 77, 78, and 79. The relationship between $\varepsilon_{\min}$ and MMD was recalculated for each band configuration. For this purpose, 108 emissivity spectra from ASTER Spectral Library were used. The result of the statistical fitting (the correlation coefficient, *r*, and the standard deviation, σ) is as follows:

$$\varepsilon_{\min} = 0.999 - 0.777(\mathrm{MMD})^{0.815}, \quad r = 0.996, \quad \sigma = 0.005. \tag{7}$$

The TES algorithm was validated using 46 *in situ* measurement points, including urban and rural areas. The results present a RMSE of 1.4 K.

Figure 5 shows two maps of LST obtained using the methodology proposed in this article, one at noon and the other at night. The images are a composition of the P01 and P02 AHS overpasses. At noon, the temperatures are between 301 and 328 K, the maximum are achieved at rural sites. During the night, the interval is of 14 K, between 290 and 304 K, with the maximum temperatures in urban zones and the minimum in rural ones. The limit of the urban zone is delimited by a black line over both overpasses.

5. SUHI and UHI effects

In this section, a comparison between the SUHI and UHI phenomena is presented.

5.1. SUHI and UHI retrieval

SUHI is defined according to Tiangco, Lagmay, and Argete (2008):

$$\mathrm{SUHI} = (\mathrm{LST})_{\mathrm{Urban}} - (\mathrm{LST})_{\mathrm{Rural}}, \tag{8}$$

where $\mathrm{LST}_{\mathrm{Urban}}$ is the average LST of the area considered as urban in the AHS images and $\mathrm{LST}_{\mathrm{Rural}}$ is the average LST of the area that results when the urban zone is removed. Limits between urban and rural zones were established according to urban contours and neighbourhood limits (black line in Figure 5).

The UHI effect was obtained as the AT differences between the average of the AT registered in the urban fixed masts ($\mathrm{AT}_{\mathrm{Urban}}$) and the AT measured in the rural fixed mast ($\mathrm{AT}_{\mathrm{Rural}}$) (Morris, Simmonds, and Plummer 2001):

$$\mathrm{UHI} = (\mathrm{AT})_{\mathrm{Urban}} - (\mathrm{AT})_{\mathrm{Rural}}. \tag{9}$$

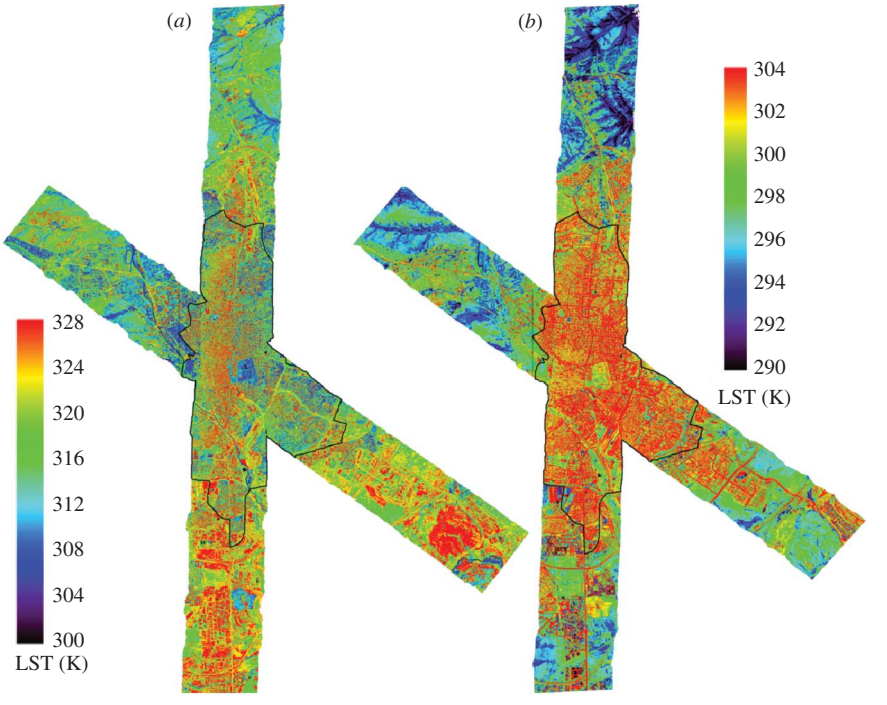

Figure 5. Map of LST applying the TES algorithm to the AHS image of 28 June 2008: (*a*) at noon and (*b*) at night. Limits of the urban zone are indicated by a fine black line. See section 3.4.1 for geographical coordinates.

5.2. Discussion

Figure 6 shows the evolution of both effects, SUHI and UHI, at the time flights. UHIs can be defined for different layers of the urban atmosphere and for various surfaces. Atmospheric heat islands may be defined for the urban canopy layer (UCL), that layer of the urban atmosphere extending upwards from the surface to approximately the mean building height, and the urban boundary layer (UBL), that layer above the UCL. On the other hand, thermal remote sensors observe the SUHI (Voogt and Oke 2003). Our fixed points of measurement are placed inside the UCL over the buildings, using masts of 3 m height.

Figure 6 displays the UHI and SUHI effects. For the SUHI phenomenon, the values are calculated for both overpasses of the AHS. Despite each overpass including different urban and rural zones (see Figure 5), the behaviour of both plots is similar.

A relevant aspect to highlight from Figure 6 is the differences observed between UHI and SUHI values retrieved simultaneously. It is observed that for noon measurements, the UHI and SUHI have maximum discrepancies, while at night we found reasonable agreement between both effects. Thus, the land surface data may indicate the UHI pattern in both surface and canopy layers during night-time. The same results were achieved by Ben-Dor and Saaroni (1997) when radiometric temperature and AT were compared for the city of Tel Aviv during night flights.

Low SUHI values (sometimes negative values) are obtained for images at noon, since the rural surfaces appear warmer than the urban ones. This negative island characterizes some inner-city urban areas, such as Madrid, in the middle of the day due to the slow uptake of heat by the city and large shaded areas from the tall buildings (Voogt 2002). Note

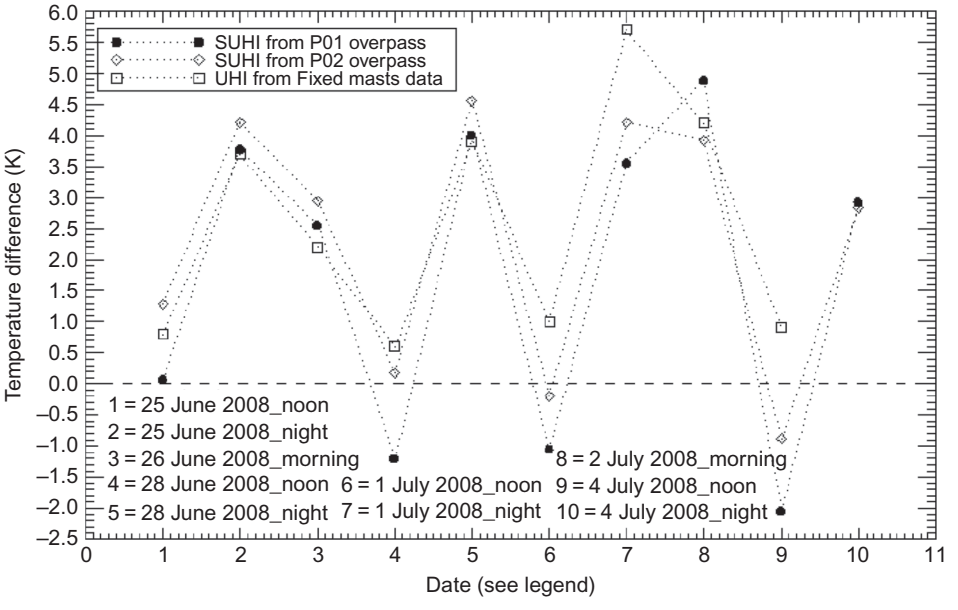

Figure 6. SUHI and UHI effects obtained during the DESIREX in the city of Madrid.

that for the UHI effect, no negative values are registered at noon, but values around 1 K are measured. So in Madrid, a decrease in the heat island effect at noon is also noticed by the atmospheric data, as it is also noticed for other cities such as Shanghai (Liu et al. 2007).

We can observe that the SUHI maximum (5 K), calculated for both AHS overpasses, and the UHI maximum (6 K) agree within 1 K, although the SUHI maximum is achieved some hours after the UHI maximum. According to the 3.2 million inhabitants of Madrid, the expected UHI maximum according to Oke (1973) is 9 K, which is 3 K over the obtained UHI maximum.

In summary, the UHI intensity is greatest at night and UHI disappears by day or the city is cooler than the rural environs, which is the same behaviour that Arnfield (2003) observed in his review of two decades of urban climate research.

6. Discomfort index

One of the consequences of the UHI effect is the influence on human health (Hart and Sailor, 2009). Because of that, it is important to study the human thermal comfort of the city. The index chosen to assess this bioclimatic comfort is the discomfort index (DI); this index estimates the effective temperature and describes the degree of discomfort at various combinations of temperature and humidity (Toy, Yilmaz, and Yilmaz 2007). DI is defined in terms of AT measured in degrees Celsius and relative humidity in percentage (f):

$$\mathrm{DI} = \mathrm{AT} - (0.55 - 0.0055f)\,(\mathrm{AT} - 14.5)\,. \tag{10}$$

From the DI temperature, 10 categories can be established (Table 5).

In this section, calculate the DI by using the LST obtained from TES algorithm instead of AT. This approximation was applied at night-time and it is acceptable at this time because the difference between AT and LST is lower than in central hours of the day, as can be

Table 5. DI categories depending on the temperature achieved (Toy, Yilmaz, and Yilmaz 2007).

DI categories	DI temperature (°C)
Hyperglacial	<−40
Glacial	–39.9 to –20
Extremely cold	–19.9 to –10
Very cold	–9.9 to –1.8
Cold	–1.7 to 12.9
Cool	13–14.9
Comfortable	15–19.9
Hot	20–26.4
Very hot	26.5–29.9
Torrid	>30

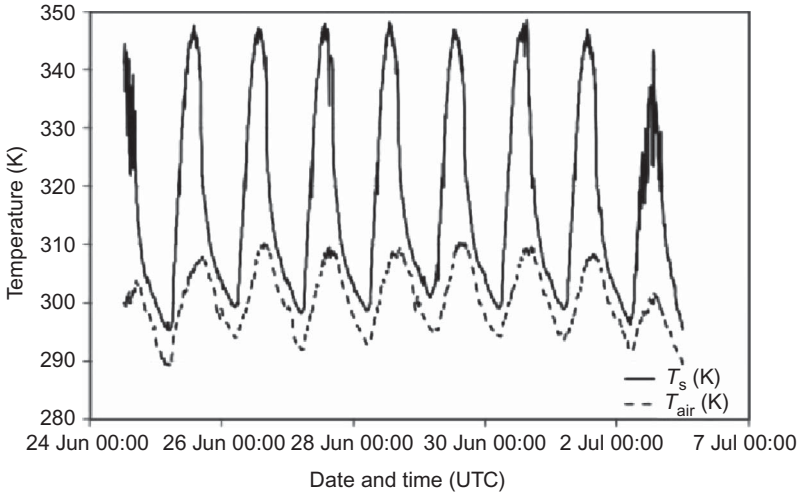

Figure 7. AT (T_{air}) and LST (T_s) registered at a fixed mast station during the DESIREX campaign.

observed in Figure 7. This figure shows the LST and AT data registered in one urban location from a fixed mast during the DESIREX 2008 campaign. It can be observed that at night-time both temperatures are similar, while near noon differences higher than 30 K are achieved. Moreover, it is interesting to compute the DI at night due to the health effects that high temperatures can cause to the inhabitants, such as insomnia events. Figure 8 shows the DI map from the composition of both AHS overpasses on the morning of 2 July, before Sun rising. It was retrieved by assuming a constant relative humidity of 32% obtained by averaging humidity data acquired from fixed masts simultaneously with the AHS flight. It is noticed that hot zones are related to the artificial surfaces, while cold and cool areas correspond to non-urban zones.

7. Summary and conclusions

The DESIREX 2008 experimental campaign has provided an excellent opportunity for collecting ground-based measurements and also for validating different algorithms for the retrieval of biophysical parameters from remote-sensing data of interest in urban areas.

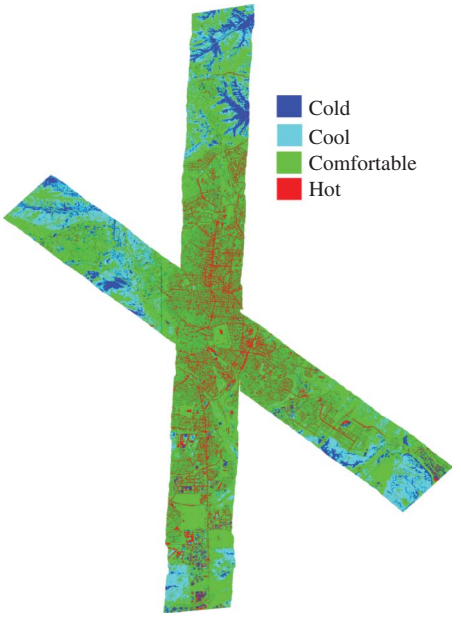

Figure 8. Map of DI retrieved from the AHS images of 2 July 2008 at 4 h UTC. See section 3.4.1 for geographical coordinates.

In this work, we mainly focused on the study of the 10 TIR bands of the AHS sensor. These bands were calibrated, obtaining a RMSE of 1 K and a Bias of 0.1 K. The main products obtained from the thermal imagery are the LST maps. We also showed that the TES algorithm shows a good performance over urban areas (RMSE of 1.4 K).

SUHI and UHI effects were measured from LST maps and AT data. The results showed a similar trend for both effects, higher values at night and lower values at noon. Thus, three main conclusions can be extracted from the results: (1) at noon, a negative heat island is registered at surface level, while a low effect around 1 K is obtained at UCL; (2) the maximum values for SUHI and UHI differ by 1 K, reaching a top value of 5 and 6 K, respectively; nevertheless, the maximum value for the UHI is recorded some hours before the SUHI maximum occurred; and (3) the differences between SUHI and UHI results are minimum during night and maximum during day, which demonstrate that the use of remote-sensing imagery during night may give the value of the heat island at surface and canopy level.

Finally, a DI map is obtained, which indicates the areas within the image that are more or less comfortable for human life. The results corroborate that most of the hot areas are inside the city, while the cooler ones are outside it.

Acknowledgements

We thank all the people and institutions taking part in the DESIREX field campaign. We also thank the ESA for financial support (project 21717/08/I-LG). During this work, Rosa Oltra-Carrió received a grant V Segles from the Universitat de València.

References

Arnfield, A. J. 2003. "Two Decades of Urban Climate Research: A Review of Turbulence, Exchanges of Energy and Water, and the Urban Heat Island." *International Journal of Climatology* 23: 1–26.

Ben-Dor, E., and H. Saaroni. 1997. "Airborne Video Thermal Radiometry as a Tool for Monitoring Microscale Structures of the Urban Heat Island." *International Journal of Remote Sensing* 18: 3039–53.

Berk, A., G. P. Anderson, P. K. Acharya, M. L. Hoke, J. H. Chetwynd, L. S. Bernstein, E. P. Shettle, M. W. Matthew, and S. M. Adler-Golden. 2003. *MODTRAN4 Version 3 Revision 1 Users' Manual*. Bedford, MA: A.F.R.L., Hanscom Air Force Base.

Fernández, F., J. P. Montávez, J. F. González-Rouco, and F. Valero. 2004. "Relación entre la estructura espacial de la isla térmica y la morfología urbana de madrid." *El Clima entre el Mar y la Montaña* A4: 641–50.

Gillespie, A., S. Rokugawa, T. Matsunaga, J. S. Cothern, S. Hook, and A. B. Kahle. 1998. "A Temperature and Emissivity Separation Algorithm for Advanced Spaceborne Thermal Emission and Reflection Radiometer (ASTER) Images." *IEEE Transactions on Geoscience and Remote Sensing* 36: 1113–26.

Guanter, L., L. Gomez-Chova, and J. Moreno. 2008. "Coupled Retrieval of Aerosol Optical Thickness, Columnar Water Vapor and Surface Reflectance Maps from ENVISAT/MERIS Data Over Land." *Remote Sensing of Environment* 112: 2898–913.

Hart, M. A., and D. J. Sailor. 2009. "Quantifying the Influence of Land-Use and Surface Characteristics on Spatial Variability in the Urban Heat Island." *Theoretical and Applied Climatology* 95: 397–406.

Hartz, D. A., L. Prashad, B. C. Hedquist, J. Golden, and A. J. Brazel. 2006. "Linking Satellite Images and Hand-Held Infrared Thermography to Observed Neighborhood Climate Conditions." *Remote Sensing of Environment* 104: 190–200.

Jasche, A., and T. Rezende. 2007. "Detection of the Urban Heat-Island Effect from a Surface Mobile Platform." *Revista de Teledetección* 27: 59–70.

Lagourade, J. P., P. Moreau, M. Irvine, J. M. Bonnefond, J. A. Voogt, and F. Solliec. 2004. "Airborne Experimental Measurements of the Angular Variations in Surface Temperature Over Urban Areas: Case Study of Marseille (France)." *Remote Sensing of Environment* 93: 443–62.

Li, J.-J., X.-R. Wang, X.-J. Wang, W.-C. Ma, and H. Zhang. 2009. "Remote Sensing Evaluation of Urban Heat Island and Its Spatial Pattern of the Shanghai Metropolitan Area, China." *Ecological Complexity* 6: 413–20.

Liu, W., C. Ji, J. Zhong, X. Jiang, and Z. Zheng. 2007. "Temporal Characteristics of the Beijing Urban Heat Island." *Theoretical and Applied Climatology* 87: 213–21.

Masson, V., L. Gomes, G. Pigeon, C. Liousse, V. Pont, J. P. Lagourade, J. Voogt, J. Salmond, T. R. Oke, J. Hidalgo, D. Legain, O. Garrouste, C. Lac, O. Connan, X. Briottet, S. Lachérade, and P. Tulet. 2008. "The Canopy and Aerosol Particles Interactions in TOulouse Urban Layer (CAPITOUL) Experiment." *Meteorology and Atmospheric Physics* 102: 135–57.

Morris, C. J. G., I. Simmonds, and N. Plummer. 2001. "Quantification of the Influences of Wind and Cloud on the Nocturnal Urban Heat Island of a Large City." *Journal of Applied Meteorology* 40: 169–82.

Najjar, G., P. P. Kastendeuch, M.-P. Stoll, J.-R. Colin, F. Nerry, N. Ringenbach, J. Bernard, A. De Hatten, R. Luhahe, and D. Viville. 2004. "Le projet Reclus. Télédétection, rayonnement et bilan d'énergie en climatologie urbaine à Strasbourg." *La Météorologie* 46: 44–50.

Oke, T. R. 1981. "Canyon Geometry and the Nocturnal Urban Heat Island: Comparison of Scale Model and Field Observations." *Journal of Climatology* 1: 237–54.

Oke, T. R. 1973. "City Size and the Urban Heat Island." *Atmospheric Environment* 7: 769–79.

Pérez-González, M. E., M. P. García-Rodríguez, and A. Guerra-Zaballos. 2003. "Análisis del clima urbano a partir de imágenes de satélite en el centro peninsular español." *Anales De Geografía De La Universidad Complutense* 23: 187–206.

Sobrino, J. A., J. C. Jiménez-Muñoz, G. Sòria, M. Gómez, A. Barella Ortiz, M. Romaguera, M. Zaragoza, Y. Julien, J. Cuenca, M. Atitar, V. Hidalgo, B. Franch, C. Mattar, A. Ruescas, L. Morales, A. Gillespie, L. Balick, Z. Su, F. Nerry, L. Peres, and R. Lionati. 2008. "Thermal Remote Sensing in the Framework of the SEN2FLEX Project: Field Measurements, Airborne Data and Applications." *International Journal of Remote Sensing* 29: 4961–91.

Sobrino, J. A., G. Sòria, R. Oltra-Carrió, J. C. Jiménez-Muñoz, M. Romaguera, J. Cuenca, V. Hidalgo, B. Franch, C. Mattar, Y. Julien, R. Bianchi, M. Paganini, J. F. Moreno, L. Alonso, A. Fernández-Renau, J. A. Gomez, E. De Miguel, O. Gutiérrez, M. Jiménez, E. Prado, R. Rodríguez-Cantano, I. Ruiz, F. Nerry, G. Najjar, P. P. Kastendeuch, M. Pujadas, F. Molero, A. Martilli, F. Salamanca, F. Fernández, E. Galán, R. Cañada, E. Hernández, J. Hidalgo, J. A. Acero, J. M. Romero, F. Moya, and L. Gimeno. 2009. "DESIREX 2008: Estudio de la isla de calor en la Ciudad de Madrid." *Revista de Teledetección* 31: 80–92.

Stathopoulou, M., A. Synnefa, C. Caralis, M. Sanamouris, T. Karless, and H. Akbari. 2009. "A Surface Heat Island Study of Athens Using High-Resolution Satellite Imagery and Measurements of the Optical and Thermal Properties of Commonly Used Building and Paving Materials." *International Journal of Sustainable Energy* 28: 59–76.

Tiangco, M., A. M. F. Lagmay, and J. Argete. 2008. "ASTER-Based Study of the Night-Time Urban Heat Island Effect in Metro Manila." *International Journal of Remote Sensing* 29: 2799–818.

Tonooka, H., F. D. Palluconi, S. J. Hook, and T. Matsunaga. 2005. "Vicarious Calibration of ASTER Thermal Infrared Bands." *IEEE Transactions on Geoscience and Remote Sensing* 43: 2733–46.

Toy, S., S. Yilmaz, and H. Yilmaz. 2007. "Determination of Bioclimatic Comfort in Three Different Land Uses in the City of Erzurum, Turkey." *Building and Environment* 42: 1315–8.

Verhoef, W., and H. Bach. 2003. "Simulation of Hyperspectral and Directional Radiance Images Using Coupled Biophysical and Atmospheric Radiative Transfer Models." *Remote Sensing of Environment* 87: 23–41.

Voogt, J. A. 2002. "Urban Heat Island." In *Encyclopedia of Global Environmental Change*, edited by T. Munn, 660–6. Chichester: Wiley.

Voogt, J. A., and T. R. Oke. 1997. "Complete Urban Surface Temperatures." *Journal of Applied Meteorology* 36: 1117–32.

Voogt, J. A., and T. R. Oke. 1998. "Radiometric Temperatures of Urban Canyon Walls Obtained from Vehicle Traverses." *Theoretical and Applied Climatology* 60: 199–217.

Voogt, J. A., and T. R. Oke. 2003. "Thermal Remote Sensing of Urban Climates." *Remote Sensing of Environment* 86: 370–84.

Yagüe, C., E. Zurita, and A. Martinez. 1991. "Statistical-Analysis of the Madrid Urban Heat-Island." *Atmospheric Environment Part B-Urban Atmosphere* 25: 327–32.